Precision Engineering 79 (2023) 173–184

Contents lists available at ScienceDirect

Precision Engineering

journal homepage: www.elsevier.com/locate/precision

Investigation of an innovative stitching-embedded characterization method for imprinting large-aperture continuous phase plates

Peng Ji [a], Bo Wang [a], Yuan Jin [a], Haitao Zhang [b], Zheng Qiao [a], Duo Li [a,b,*]

[a] Center for Precision Engineering, Harbin Institute of Technology, Harbin, 150001, China
[b] State Key Laboratory of Applied Optics, Changchun Institute of Optics, Fine Mechanics and Physics, Chinese Academy of Sciences, Changchun, Jilin, 130033, China

ARTICLE INFO

Keywords:
Large-aperture continuous phase plates
Sub-aperture stitching
Characterization

ABSTRACT

In high-power laser systems, the large-aperture continuous phase plates (CPPs) are designed and fabricated with continuous varying structured topography to serve as the class of phase-modulating beam-conditioning optics. To achieve better optical performance, its fabrication highly depends on the reiterative figuring to eliminate the form error relative to the designed CPP surface. However, the characteristics of large aperture and complex structured topography make the quality inspection of CPPs still challenging. A typical inspection process includes measuring the CPPs with the sub-aperture stitching technique, followed by the characterization procedure with respect to the CPP design description. This paper proposes an innovative stitching-embedded characterization method for imprinting the large-aperture CPPs, which combines the sub-aperture stitching and characterization procedure together. First, the concept and mathematical model of the stitching-embedded characterization method is presented. Then, both numerical simulations and experiments were undertaken to verify the proposed method, and the results demonstrate its feasibility and reasonability to provide the more reliable form error evaluation while simplify the analysis procedure compared with the conventional inspection process.

1. Introduction

The large-aperture continuous phase plates (CPPs) have now been extensively applied in the high-power laser systems by its outstanding performance of beam shaping and smoothing [1,2]. The CPP surface is featured with the vertical fluctuation of small amplitudes, which can be essentially regarded as a plane superposed by the microstructure with several micrometers [3]. Computer controlled optical surfacing (CCOS) technologies, such as magnetorheological finishing (MRF) [4], ion beam figuring (IBF) [5], bonnet polishing (BP) [6] and plasma processing [7], are often adopted for imprinting the continuously varying structured topography of CPPs in high precision. Typically, the height error in the range of tens of nanometers is necessary for the optical performance of CPPs [8]. The specific tight precision requirements give much more challenges to the fabrication of large-aperture CPPs, which is generally not a once-through procedure [5]. For the complexity of surface topography, the fabrication of large-aperture CPPs is often a repetitive closed-loop that comprises figuring process, and quality inspection.

Different from the general planar optics, the quality inspection of large-aperture CPPs is more complicated. First, the direct full-aperture surface measurement by the large-aperture interferometric system is strictly limited by the low lateral resolution, which is only suitable for the general planar optics to check its flatness. Considering the abundant middle-frequency components in CPPs, the full-aperture test may result in the loss of wavefront information. Second, the measurement result of imprinted CPP surface cannot be directly applied to the form error evaluation, while this issue does not occur for the general planar optics in quality inspection. For imprinting CPPs, the existing designed surface is regarded as the reference, which is constantly compared with measured CPP surface in each processing iteration. By contrast, the figuring of the general planar optics is only targeted at improving the flatness, and the measurement result gives rightly the difference with respect to the reference flat.

In the past decades, the concept of sub-aperture stitching technique [9,10] is proposed and highly developed in optical surface metrology to address the issue of measuring the large-aperture optics with the single limited field of view (FOV). With the advanced stitching algorithms, this technique can reconstruct the full-aperture surface topography based on the multiple overlapping regions of different sub-apertures by removing their relative positional deviation. The development of stitching technique makes the measurement of large-aperture CPPs accessible and practical, which extends the measuring size and range, but preserves the

* Corresponding author. P.O. Box 413, Harbin, 150001, China.
E-mail address: liduo@hit.edu.cn (D. Li).

https://doi.org/10.1016/j.precisioneng.2022.10.004
Received 11 July 2022; Received in revised form 8 September 2022; Accepted 11 October 2022
Available online 14 October 2022

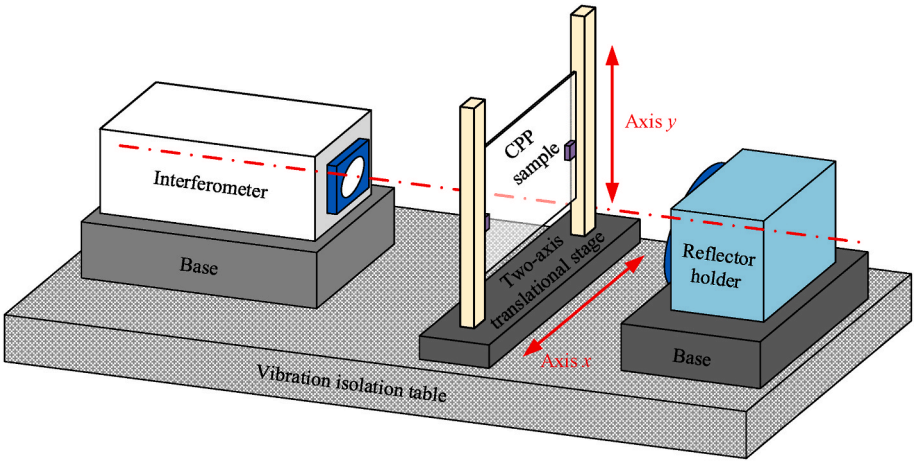

Fig. 1. Typical experiment setup of the large-aperture CPPs.

native lateral resolution. It is reported that Beau et al. reconstructed the CPP phase profile with a size of 383 mm × 398 mm with five sub-apertures of 300 mm diameter [11]. Despite of the convenience, one obvious shortcoming is that the original proposed stitching algorithm only removes the relative piston and tip-tilt of each sub-aperture without considering the influence of lateral shift or positioning error [12]. For improving the flatness of the large-aperture planar optics, more attention is paid to the low-frequency form error, which makes the lateral error at pixel or subpixel level neglectable while positioning the sub-apertures. Generally, the wavefront slope of the low-frequency form error is sufficient small and will not introduce remarkable phase error. By contrast, the form error of CPPs is typically featured with relatively higher frequency and larger vertical fluctuation, leading to the large slope that is sensitive to the lateral misalignment-induced error. To solve this, it is imperative to develop the complete stitching algorithm involving six degrees of freedom (DOFs). For example, Chen et al. proposed a stitching algorithm with quasi-planar free-form surface registration to eliminate the lateral misalignment-induced error [13].

Despite the measurement result acquired by the sub-aperture stitching technique, the characterization of CPPs cannot be conducted by directly subtracting the designed surface from the measured data [14]. Similar to the stitching procedure of any two sub-apertures, there also exists the difference in coordinates between the designed and measured CPP surface, which needs to be solved by freeform surface matching or registration. Nowadays, great strides have been made in the characterization methods of ultra-precision freeform surfaces [15,16], but the developed algorithms cannot be directly applied for imprinting CPPs. Although they essentially belong to the optimization problem, the original criterion of minimum Euclidean distance should be modified as the target of finding the optimal rigid body transformation with six DOFs to minimize the height error normal to the plane. From another perspective, the height error is the key to impact the optical performance of CPPs. Besides, it's worth noting that the characterization of CPPs mainly serves for the generation of removal distribution for the next figure iteration. This kind of problem was investigated by Chen et al. and the parametric registration method of cross test error maps for optical surfaces was successfully developed [17]. Our research group also presented the two-phase characterization method for imprinting CPPs [14], which can provide the reliable form error evaluation with sub-nanometer accuracy.

In summary, based on the sub-aperture test, the conventional quality inspection of the imprinted large-aperture CPPs consists of two

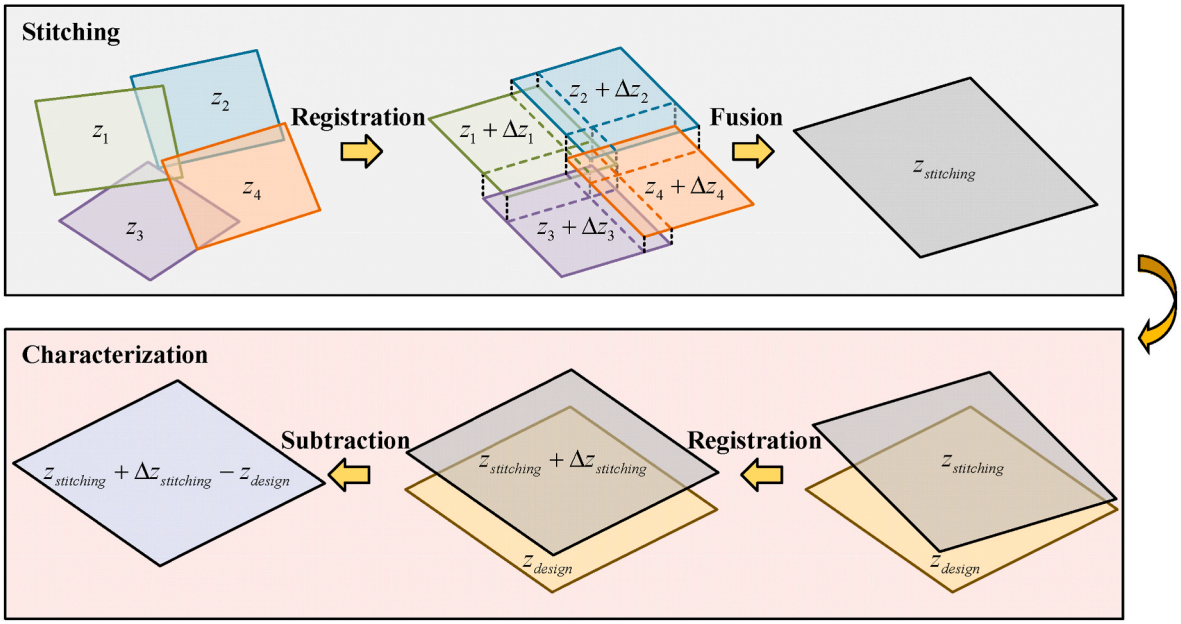

Fig. 2. Conventional quality inspection process of CPPs.

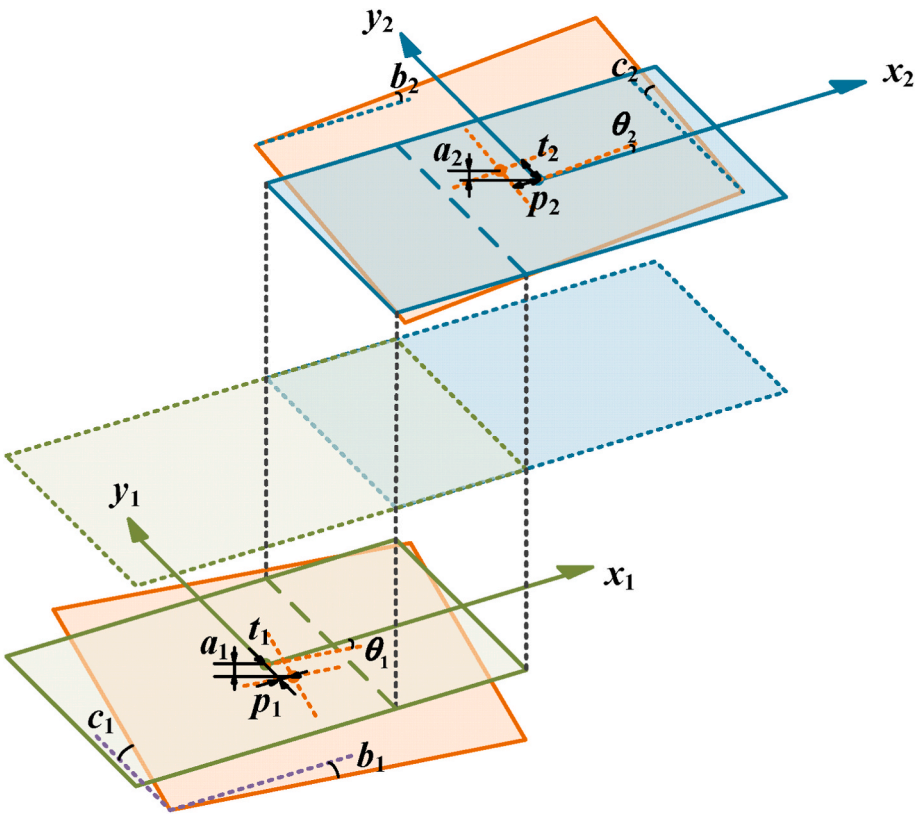

Fig. 3. Stitching principle of two sub-apertures.

successive analysis stages, stitching and characterization, which is time-consuming and complicated. Besides, considering the serial procedure, the analysis error in the last stage will be transferred to the next stage. This undoubtedly leads to the uncertainty of form error evaluation, which is sensitive to the error accumulation.

In essence, the stitching and characterization are both registration-based problems, and focus on eliminating the misalignment of different surfaces. To further improve the efficiency, this paper proposes an innovative stitching-embedded characterization method for imprinting the large-aperture CPPs, which integrates the two independent analysis stages together. In this paper, the concept of the stitching-embedded characterization method is first introduced and compared with the conventional quality inspection of CPPs. Second, its principle is discussed by establishing the mathematical model. Then, the simulation was conducted to verify the feasibility and reasonability of the proposed method. Finally, the experiment was implemented to investigate its performance and compared with the conventional quality inspection of CPPs.

2. Concept and comparison

The typical experiment setup of the large-aperture CPPs is given in Fig. 1, which is a testing system that measuring the large planar transmitted wavefronts. It mainly consists of the interferometer, two-axis translational stage, and reflector in the holder. Generally, the vibration isolation table is adopted to make the interferometric system more stable and repeatable. The CPP sample is fixed on the two-axis translational stage, which is controlled by the computer to move to acquire all the sub-aperture maps at different positions. Based on this, the conventional quality inspection of CPPs starts from the sub-aperture stitching, and ends with the characterization procedure, as shown in Fig. 2. The registration of all the sub-aperture maps is first implemented to eliminate the mutual misalignment, which is aimed to minimize the overlapping inconsistency. According to the solved rigid transformation parameters, all the sub-aperture maps are adjusted and fused together to generate the full-aperture CPP surface topography. When the sub-aperture stitching completes, the characterization procedure is performed by precisely aligning the full-aperture map to compare with the designed CPP surface, which is the targeting reference in every quality inspection. When the misalignment is fully eliminated, the removal distribution generation is finally conducted by adding the height-inverted topographical surface of the designed CPP to the measurement data of the imprinted CPP surface [5].

Due to the sensibility of lateral misalignment-induced error for imprinting CPPs, the original proposed stitching algorithm become uncompetitive with the complete stitching algorithm involving six DOFs. Similarly, the six positional deviations should also be incorporated in the characterization of CPPs. Whether stitching or characterization, the height change Δz of CPPs can be simply related to the misalignment by the linear approximation as below [18],

$$\Delta z = a + bx + cy + p\frac{\partial z}{\partial x} + t\frac{\partial z}{\partial y} + \theta\left(x\frac{\partial z}{\partial y} - y\frac{\partial z}{\partial x}\right) \tag{1}$$

where a, b and c denote the coefficients of piston, tip and tilt, p and t are the lateral shifts, and θ is the small clocking angle. The partial derivatives are the slopes of CPP topography. The core of stitching algorithm can be summarized as the least-squares problem for finding the unknown six parameters of every sub-aperture,

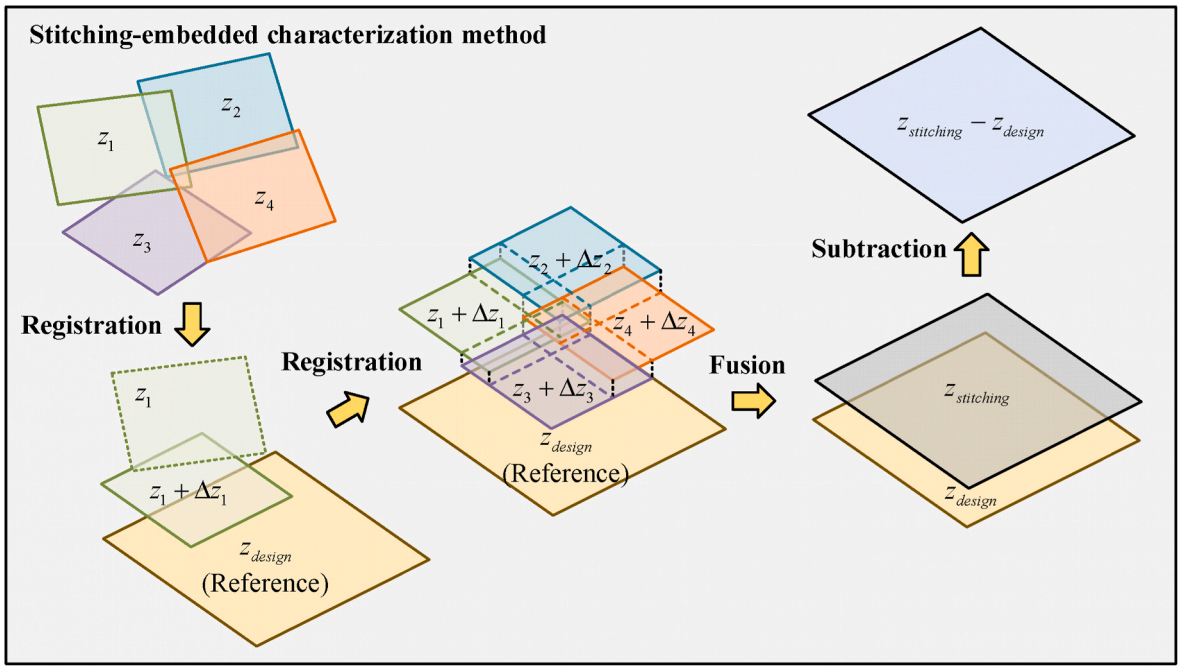

Fig. 4. Quality inspection of CPPs by the stitching-embedded characterization method.

$$\min F_{stitching} = \min \sum_{i=1}^{M-1} \sum_{k=i+1}^{M} \sum_{jo=1}^{{}^{ik}N_o} \left(\left({}^{ik}z_{i,jo} + \Delta z_{i,jo} \right) - \left({}^{ik}z_{k,jo} + \Delta z_{k,jo} \right) \right)^2 \tag{2}$$

The left superscript '*ik*' indicates the overlap between the sub-apertures i and k, and ${}^{ik}N_o$ is the number of overlapping point pairs. For example, the stitching principle of two sub-apertures is illustrated in Fig. 3. To avoid the problem of error stack-up, the simultaneous stitching mode, instead of the sequential stitching mode, is preferred, where all the sub-aperture maps are processed at the same time. Equation (2) can be further transformed into,

$$\underbrace{\begin{bmatrix} A_{12} & -A_{12} & 0 & \cdots & 0 & \cdots & 0 & \cdots & 0 & 0 \\ A_{13} & 0 & -A_{13} & \cdots & 0 & \cdots & 0 & \cdots & 0 & 0 \\ \vdots & \vdots & \vdots & \ddots & \vdots & \ddots & \vdots & \ddots & \vdots & \vdots \\ 0 & 0 & 0 & \cdots & A_{ik} & \cdots & -A_{ik} & \cdots & 0 & 0 \\ \vdots & \vdots & \vdots & \ddots & \vdots & \ddots & \vdots & \ddots & \vdots & \vdots \\ 0 & 0 & 0 & \cdots & 0 & \cdots & 0 & \cdots & A_{M-1,M} & -A_{M-1,M} \end{bmatrix}}_{\mathbf{A}} \underbrace{\begin{bmatrix} q_1 \\ q_2 \\ q_3 \\ \vdots \\ q_i \\ \vdots \\ q_k \\ \vdots \\ q_{M-1} \\ q_M \end{bmatrix}}_{\mathbf{q}} = \underbrace{\begin{bmatrix} z_{12} \\ z_{13} \\ \vdots \\ z_{ik} \\ \vdots \\ z_{M-1,M} \end{bmatrix}}_{\mathbf{z}} \tag{3}$$

where the submatrices are defined as,

$$A_{ik} = \begin{bmatrix} 1 & x_{i,1} & y_{i,1} & \dfrac{\partial z_{i,1}}{\partial x_{i,1}} & \dfrac{\partial z_{i,1}}{\partial y_{i,1}} & x_{i,1}\dfrac{\partial z_{i,1}}{\partial y_{i,1}} - y_{i,1}\dfrac{\partial z_{i,1}}{\partial x_{i,1}} \\ 1 & x_{i,2} & y_{i,2} & \dfrac{\partial z_{i,2}}{\partial x_{i,2}} & \dfrac{\partial z_{i,2}}{\partial y_{i,2}} & x_{i,2}\dfrac{\partial z_{i,2}}{\partial y_{i,2}} - y_{i,2}\dfrac{\partial z_{i,2}}{\partial x_{i,2}} \\ \vdots & \vdots & \vdots & \vdots & \vdots & \vdots \\ 1 & x_{i,jo} & y_{i,jo} & \dfrac{\partial z_{i,jo}}{\partial x_{i,jo}} & \dfrac{\partial z_{i,jo}}{\partial y_{i,jo}} & x_{i,jo}\dfrac{\partial z_{i,jo}}{\partial y_{i,jo}} - y_{i,jo}\dfrac{\partial z_{i,jo}}{\partial x_{i,jo}} \\ \vdots & \vdots & \vdots & \vdots & \vdots & \vdots \\ 1 & x_{i,{}^{ik}N_o} & y_{i,{}^{ik}N_o} & \dfrac{\partial z_{i,{}^{ik}N_o}}{\partial x_{i,{}^{ik}N_o}} & \dfrac{\partial z_{i,{}^{ik}N_o}}{\partial y_{i,{}^{ik}N_o}} & x_{i,{}^{ik}N_o}\dfrac{\partial z_{i,{}^{ik}N_o}}{\partial y_{i,{}^{ik}N_o}} - y_{i,{}^{ik}N_o}\dfrac{\partial z_{i,{}^{ik}N_o}}{\partial x_{i,{}^{ik}N_o}} \end{bmatrix} \tag{4}$$

$$-A_{ik} = \begin{bmatrix} -1 & -x_{k,1} & -y_{k,1} & -\dfrac{\partial z_{k,1}}{\partial x_{k,1}} & -\dfrac{\partial z_{k,1}}{\partial y_{k,1}} & -x_{k,1}\dfrac{\partial z_{k,1}}{\partial y_{k,1}} + y_{k,1}\dfrac{\partial z_{k,1}}{\partial x_{k,1}} \\ -1 & -x_{k,2} & -y_{k,2} & -\dfrac{\partial z_{k,2}}{\partial x_{k,2}} & -\dfrac{\partial z_{k,2}}{\partial y_{k,2}} & -x_{k,2}\dfrac{\partial z_{k,2}}{\partial y_{k,2}} + y_{k,2}\dfrac{\partial z_{k,2}}{\partial x_{k,2}} \\ \vdots & \vdots & \vdots & \vdots & \vdots & \vdots \\ -1 & -x_{k,jo} & -y_{k,jo} & -\dfrac{\partial z_{k,jo}}{\partial x_{k,jo}} & -\dfrac{\partial z_{k,jo}}{\partial y_{k,jo}} & -x_{k,jo}\dfrac{\partial z_{k,jo}}{\partial y_{k,jo}} + y_{k,jo}\dfrac{\partial z_{k,jo}}{\partial x_{k,jo}} \\ \vdots & \vdots & \vdots & \vdots & \vdots & \vdots \\ -1 & -x_{k,{}^{ik}N_o} & -y_{k,{}^{ik}N_o} & -\dfrac{\partial z_{k,{}^{ik}N_o}}{\partial x_{k,{}^{ik}N_o}} & -\dfrac{\partial z_{k,{}^{ik}N_o}}{\partial y_{k,{}^{ik}N_o}} & -x_{k,{}^{ik}N_o}\dfrac{\partial z_{k,{}^{ik}N_o}}{\partial y_{k,{}^{ik}N_o}} + y_{k,{}^{ik}N_o}\dfrac{\partial z_{k,{}^{ik}N_o}}{\partial x_{k,{}^{ik}N_o}} \end{bmatrix} \tag{5}$$

$$q_i = [a_i, b_i, c_i, p_i, t_i, \theta_i]^{\mathrm{T}} \tag{6}$$

$$z_{ik} = \left[z_{i,1} - z_{k,1}, z_{i,2} - z_{k,2}, \cdots, z_{i,jo} - z_{k,jo}, \cdots, z_{i,{}^{ik}N_o} - z_{k,{}^{ik}N_o} \right]^{\mathrm{T}} \tag{7}$$

By solving Eq. (3), the unknown six parameters can be acquired according to,

$$\mathbf{q} = \left(\mathbf{A}^{\mathrm{T}} \mathbf{A} \right)^{-1} \mathbf{A}^{\mathrm{T}} \mathbf{z} \tag{8}$$

where $(\cdot)^{\mathrm{T}}$ indicates the matrix transpose operation and $(\cdot)^{-1}$ stands for the matrix inverse operation.

As for the characterization of CPPs, it can be considered as the simplified stitching problem with two completely overlapped sub-apertures, but one of them is the designed CPP surface. If z_{design} and $z_{stitching}$ represent the designed CPP surface and the full-aperture measured CPP surface from the sub-aperture test, the corresponding optimization target of the least-squares problem is modified as,

$$\min F_{characterization} = \min \sum_{jo=1}^{N_o} \left(z_{stitching,jo} + \Delta z_{stitching,jo} - z_{design,jo} \right)^2 \tag{9}$$

From abovementioned analysis, the sub-aperture stitching and characterization procedure in the conventional quality inspection of CPPs are completely independent. The concept of 'stitching, and then characterization' simply draws on the evaluation of figuring large-

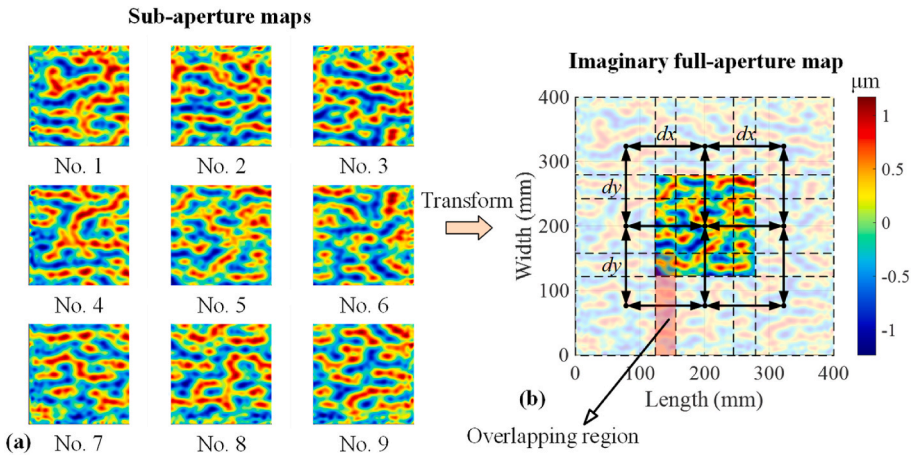

Fig. 5. Illustration of transforming all the sub-aperture maps. (a) Before transforming; (b) After transforming (take the central sub-aperture map as the example).

aperture planar optics, where there only exists the mutual registration of all sub-apertures. Its necessity lies in the fact that the characterization of the planar optics can be directly conducted without any registration. When the piston and tip-tilt is removed by least-squares plane fitting, the form error has been latently determined. This way, the sub-aperture stitching only centers on dealing with the sub-apertures themselves.

If we reexamine the conventional quality inspection of CPPs, it can be found that the sub-aperture stitching is essential and irreducible. In two successive analysis stages, all the sub-aperture maps can be considered to be individually adjusted twice. The rigid transformation matrices of each sub-aperture maps are different in the sub-aperture stitching but the same in the characterization procedure. Further, if the two adjustments of every sub-aperture map are integrated together, the quality inspection of CPPs will be largely simplified. This way, like the evaluation of figuring large-aperture planar optics, the sub-aperture stitching and characterization procedure are combined together. In another word, the full-aperture form error of the imprinted CPPs can be directly acquired by the sub-aperture stitching. Based on this concept, we propose the stitching-embedded characterization method for quality inspection of CPPs, as shown in Fig. 4. Its peculiarity is to integrate the designed CPP surface as the reference into the sub-aperture stitching. This way, all the sub-apertures are only adjusted once, and the acquired full-aperture map has been latently aligned with the designed CPP surface. Compared with the conventional method, the stitching-embedded characterization method is significantly efficient. Besides, benefit from the combination of the original two steps, the error accumulation between the two successive stages is eliminated, which makes the form error evaluation more accurate and reliable. The detailed principle is fully discussed in Section 3.

3. Principle of the stitching-embedded characterization method

3.1. Sub-aperture pre-processing

Since all the sub-aperture maps are obtained under different coordinate systems, the stitching procedure cannot be directly conducted. First, multiple blank full-aperture data matrices are established, and then respectively padded with every sub-aperture map according to the nominal positions. Through this, all the sub-aperture maps are transformed into the global coordinate system. For example, the targeting full-aperture CPP map with a size of 400 mm × 400 mm is divided into nine sub-apertures, and each of them is 160 mm× 160 mm, as shown in Fig. 5 (a). Under this condition, the central sub-aperture is generally selected to be fixed and primarily padded in the blank full-aperture data matrix. According to the nominal position of every sub-aperture, the corresponding pixel distance can be calculated with the size of single pixel, which is used to approximately position every sub-aperture map. Compared with the precise alignment, this transformation can be regarded as the coarse registration and only serves for determining the overlapping region, as shown in Fig. 5 (b).

Similarly, the height value of the designed CPP surface can be padded in another blank full-aperture matrix with the same size before, as shown in Fig. 6. This way, with the help of the prior knowledge, all the sub-apertures can be approximately matched with the corresponding

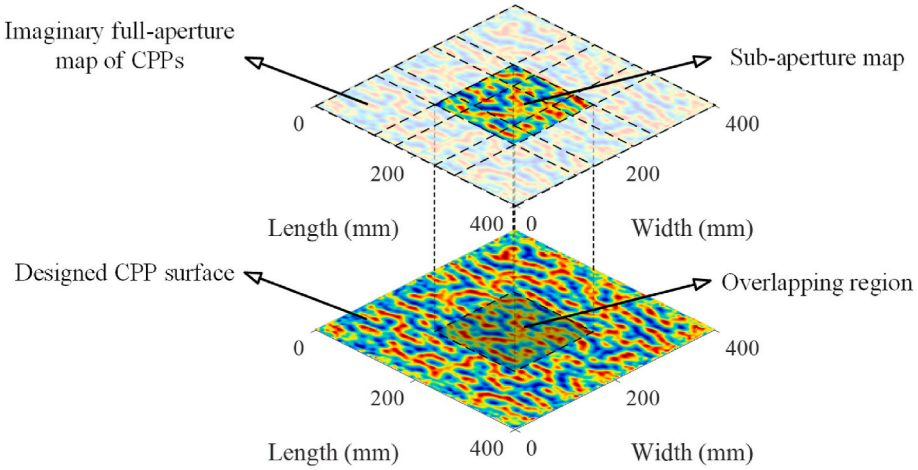

Fig. 6. Illustration of the comparison between the full-aperture map of CPPs and the designed CPP surface.

designed surface. This operation lays the great foundation for establishing the overlapping point pairs between the measured and designed CPP surface. And their value difference can be used to effectively characterize the registration performance.

3.2. Registration of the standard sub-aperture maps

In the original proposed stitching algorithm, all the sub-aperture maps tend to be aligned and stitched based on one of them set as the standard. In the concept of Section 2, if all the sub-aperture maps achieve the registration with the designed CPP surface at one go, each of them can be selected as the global standard to implement the registration first. The sub-aperture preprocessing makes all the registration only focus on dealing with the height value, because all the overlapping point pairs share the same lateral pixel position. Suppose that the standard sub-aperture map and the designed CPP surface are denoted by $\mathbf{P}_1 = \{(x_j, y_j, z_{1,j}) \big| j = 1, 2, \cdots, N_1\}$ and $\mathbf{P}_2 = \{(x_j, y_j, z_{2,j}) \big| j = 1, 2, \cdots, N_2\}$. The registration problem of the standard sub-aperture map is expressed as,

$$\min F = \min \sum_{jo=1}^{N_o} \left(z_{1,jo} + a + bx_{jo} + cy_{jo} + p\frac{\partial z_{1,jo}}{\partial x_{jo}} + t\frac{\partial z_{1,jo}}{\partial y_{jo}} + \theta\left(x_{jo}\frac{\partial z_{1,jo}}{\partial y_{jo}} - y_{jo}\frac{\partial z_{1,jo}}{\partial x_{jo}} \right) - z_{2,jo} \right)^2 \tag{10}$$

By differentiating Eq. (10), the unknown six parameters can be calculated by solving the matrix equation,

$$\begin{bmatrix} N_o & \sum x & \sum y & \sum \frac{\partial z_1}{\partial x} & \sum \frac{\partial z_1}{\partial y} & \sum f \\ \sum x & \sum x^2 & \sum xy & \sum x\frac{\partial z_1}{\partial x} & \sum x\frac{\partial z_1}{\partial y} & \sum xf \\ \sum y & \sum yx & \sum y^2 & \sum y\frac{\partial z_1}{\partial x} & \sum y\frac{\partial z_1}{\partial y} & \sum yf \\ \sum \frac{\partial z_1}{\partial x} & \sum \frac{\partial z_1}{\partial x}x & \sum \frac{\partial z_1}{\partial x}y & \sum \left(\frac{\partial z_1}{\partial x}\right)^2 & \sum \frac{\partial z_1}{\partial x}\frac{\partial z_1}{\partial y} & \sum \frac{\partial z_1}{\partial x}f \\ \sum \frac{\partial z_1}{\partial y} & \sum \frac{\partial z_1}{\partial y}x & \sum \frac{\partial z_1}{\partial y}y & \sum \frac{\partial z_1}{\partial y}\frac{\partial z_1}{\partial x} & \sum \left(\frac{\partial z_1}{\partial y}\right)^2 & \sum \frac{\partial z_1}{\partial y}f \\ \sum f & \sum fx & \sum fy & \sum f\frac{\partial z_1}{\partial x} & \sum f\frac{\partial z_1}{\partial y} & \sum f^2 \end{bmatrix} \begin{bmatrix} a \\ b \\ c \\ p \\ t \\ \theta \end{bmatrix} = \begin{bmatrix} \sum (z_2 - z_1) \\ \sum x(z_2 - z_1) \\ \sum y(z_2 - z_1) \\ \sum \frac{\partial z_1}{\partial x}(z_2 - z_1) \\ \sum \frac{\partial z_1}{\partial y}(z_2 - z_1) \\ \sum f(z_2 - z_1) \end{bmatrix} \tag{11}$$

$$f(x, y, z_1) = \left(x\frac{\partial z_1}{\partial y} - y\frac{\partial z_1}{\partial x} \right) \tag{12}$$

where '$\sum(\cdot)$' is the sum of the value in the bracket ($jo = 1, 2, \cdots, N_o$), and N_o is the number of overlapping points. So far, the standard sub-aperture map can be precisely adjusted with the six parameters determined, and completely aligned with the corresponding partial designed CPP surface.

3.3. Stitching-embedded characterization

For the stitching of the sub-aperture maps, the simultaneous stitching mode is still preferred to avoid the problem of error stack-up. Different the original stitching algorithm, the designed CPP surface is introduced to serve as the reference and align every sub-aperture maps. This way, after the primary registration of the standard sub-aperture map, minimizing the overlapping inconsistency of all the sub-aperture maps automatically achieves the precise alignment to the designed CPP surface. If z_i indicates the sub-aperture maps, the alignment of each sub-aperture map can be mathematically implemented with,

$$\Delta z_i = a_i + b_i x + c_i y + p_i\frac{\partial z_d}{\partial x} + t_i\frac{\partial z_d}{\partial y} + \theta_i\left(x\frac{\partial z_d}{\partial y} - y\frac{\partial z_d}{\partial x} \right) \tag{13}$$

where z_d is the corresponding overlapping region of the designed CPP surface. Equation (13) can be explained by the equivalence of aligning the designed CPP surface, which is the same as the use of each sub-aperture map itself. Based on this, in the simultaneous stitching mode, the least-squares problem is summarized as,

$$\min F = \min \sum_{i=1}^{M} \sum_{k=1}^{M} \sum_{jo=1}^{{}^{ik}N_o} \left(\left({}^{ik}z_{i,jo} + \Delta z_{i,jo} \right) - \left({}^{ik}z_{k,jo} + \Delta z_{k,jo} \right) \right)^2 \tag{14}$$

where there are M sub-aperture maps. Considering the completed registration of the mth sub-aperture map as the standard one, Eq. (15) should be added as,

$$\Delta z_m = 0 \tag{15}$$

Taking the differentiation of Eq. (14) with respect to six unknown parameters, the final least-squares matrix equation can be acquired as,

$$\left[\left(\sum_{k=1}^{M} \mathbf{P}_{ik} \right)_i \right] = \left[\left(\mathbf{Q}_{ij} - \delta_{ij} \sum_{k=1}^{M} \mathbf{Q}_{ik} \right)_{ij} \right] [(\mathbf{R}_i)_i] \tag{16}$$

Equation (16) is composed of three cell arrays, and the size are $(M-1) \times 1$, $(M-1) \times (M-1)$ and $(M-1) \times 1$ from left to right. And i and j are the integers from 1 to M excluding m. Further, Eq. (16) can be established by,

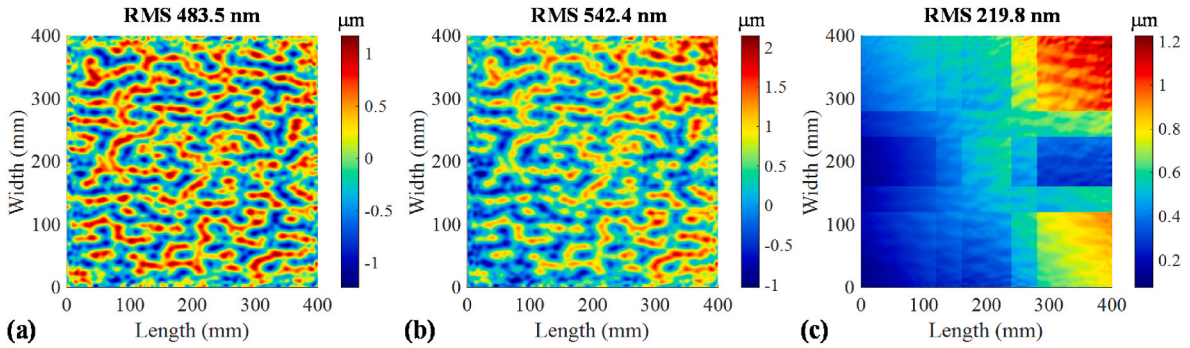

Fig. 7. Direct data fusion with the original sub-aperture maps. (a) Designed CPP surface; (b) Full-aperture map by direct data fusion; (c) Difference between (a) and (b).

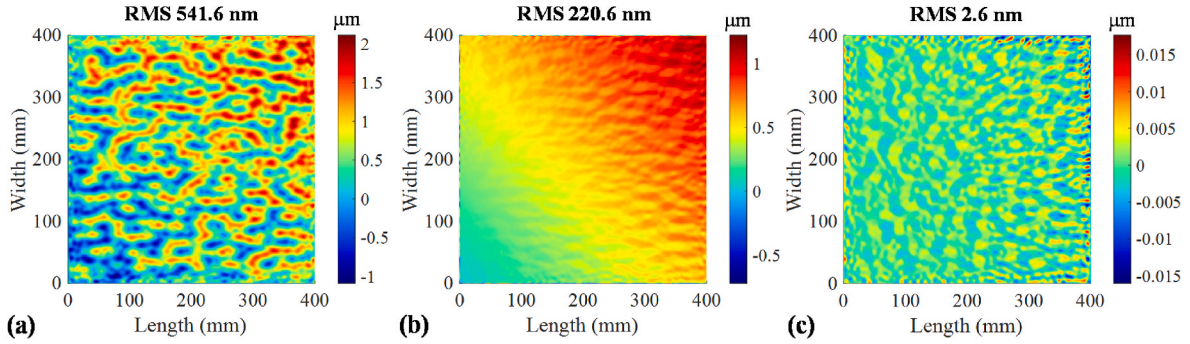

Fig. 8. Simulation results with the conventional method. (a) Full-aperture map after stitching; (b) Form error by directly subtracting the designed CPP surface from (a); (c) Form error acquired by the following registration with the designed CPP surface.

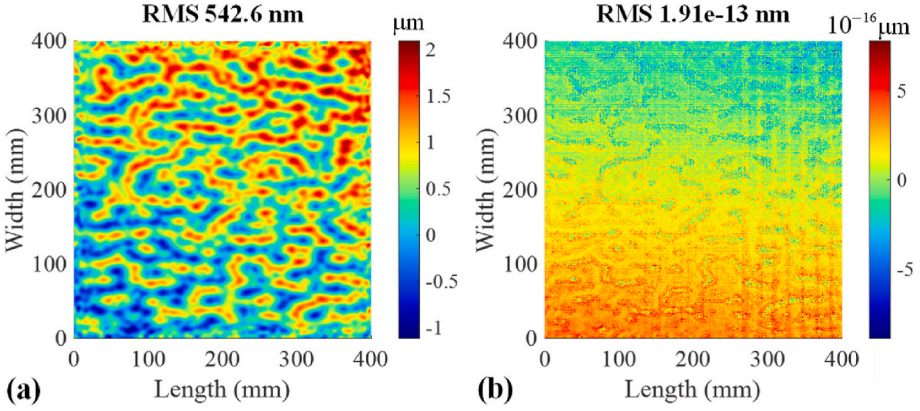

Fig. 9. Comparison simulation with only regular characterization. (a) Misaligned CPP surface; (b) Form error acquired by the regular characterization.

$$\mathbf{P}_{ik}=\left[\sum_{i\cap k}\Delta z,\sum_{i\cap k}x\Delta z,\sum_{i\cap k}y\Delta z,\sum_{i\cap k}\frac{\partial z_d}{\partial x}\Delta z,\sum_{i\cap k}\frac{\partial z_d}{\partial y}\Delta z,\sum_{i\cap k}f\Delta z\right]^T \tag{17}$$

$$\mathbf{Q}_{ik}=\begin{cases}\begin{bmatrix} {}^{ik}N_o & \sum_{i\cap k}x & \sum_{i\cap k}y & \sum_{i\cap k}\frac{\partial z_d}{\partial x} & \sum_{i\cap k}\frac{\partial z_d}{\partial y} & \sum_{i\cap k}f \\ \sum_{i\cap k}x & \sum_{i\cap k}x^2 & \sum_{i\cap k}xy & \sum_{i\cap k}x\frac{\partial z_d}{\partial x} & \sum_{i\cap k}x\frac{\partial z_d}{\partial y} & \sum_{i\cap k}xf \\ \sum_{i\cap k}y & \sum_{i\cap k}yx & \sum_{i\cap k}y^2 & \sum_{i\cap k}y\frac{\partial z_d}{\partial x} & \sum_{i\cap k}y\frac{\partial z_d}{\partial y} & \sum_{i\cap k}yf \\ \sum_{i\cap k}\frac{\partial z_d}{\partial x} & \sum_{i\cap k}\frac{\partial z_d}{\partial x}x & \sum_{i\cap k}\frac{\partial z_d}{\partial x}y & \sum_{i\cap k}\left(\frac{\partial z_d}{\partial x}\right)^2 & \sum_{i\cap k}\frac{\partial z_d}{\partial x}\frac{\partial z_d}{\partial y} & \sum_{i\cap k}\frac{\partial z_d}{\partial x}f \\ \sum_{i\cap k}\frac{\partial z_d}{\partial y} & \sum_{i\cap k}\frac{\partial z_d}{\partial y}x & \sum_{i\cap k}\frac{\partial z_d}{\partial y}y & \sum_{i\cap k}\frac{\partial z_d}{\partial y}\frac{\partial z_d}{\partial x} & \sum_{i\cap k}\left(\frac{\partial z_d}{\partial y}\right)^2 & \sum_{i\cap k}\frac{\partial z_d}{\partial y}f \\ \sum_{i\cap k}f & \sum_{i\cap k}fx & \sum_{i\cap k}fy & \sum_{i\cap k}f\frac{\partial z_d}{\partial x} & \sum_{i\cap k}f\frac{\partial z_d}{\partial y} & \sum_{i\cap k}f^2 \end{bmatrix}, i\neq k \\ \begin{bmatrix} 0&0&0&0&0&0\\ 0&0&0&0&0&0\\ 0&0&0&0&0&0\\ 0&0&0&0&0&0\\ 0&0&0&0&0&0\\ 0&0&0&0&0&0 \end{bmatrix}, i=k \end{cases} \tag{18}$$

$$\mathbf{R}_i=[a_i,b_i,c_i,p_i,t_i,\theta_i]^T \tag{19}$$

$$f(x,y,z_d)=\left(x\frac{\partial z_d}{\partial y}-y\frac{\partial z_d}{\partial x}\right) \tag{20}$$

$$\delta_{ij}=\begin{cases}1, i=j\\ 0, i\neq j\end{cases} \tag{21}$$

So far, all the sub-aperture maps except the standard one can be stitched together, which have been aligned to the designed CPP surface. The quality inspection of CPPs is conducted by directly comparing the fused full-aperture map with the designed CPP surface. Further, the form error of the imprinted CPPs is determined by,

$$z_e=z_{stitching}-z_{design} \tag{22}$$

4. Numerical simulation and verification

4.1. Characterization accuracy

To verify the characterization accuracy of the proposed stitching-embedded characterization method, the simulation was conducted to compare with the conventional quality inspection of CPPs, where the complete stitching algorithm involving six DOFs and the regular characterization were successively performed. 'Direct characterization after stitching' is the unique peculiarity in the proposed stitching-embedded characterization method. Considering this, no form error was introduced in this simulation, which was designed to be the pure virtual stitching test and validate the characterization accuracy. The designed CPP surface and sub-aperture division was the same as Section 3.1. The pixel size is 0.2 mm. All the translational and rotational misalignment (six DOFs) were set to be the random value within 0.1 mm and 0.1°. Without loss of generality, the form error is characterized by the root-mean-square (RMS).

First, the original sub-aperture maps were directly fused together without any registration, as shown in Fig. 7. Compared with the designed CPP surface, there obviously exists the discontinuity in the full-aperture map. According to their difference shown in Fig. 7 (c), all the sub-aperture is misaligned with each other, not to mention the designed CPP surface. The false form error is determined to be RMS 219.8 nm, which deviates greatly from the theoretical zero value.

With the complete stitching algorithm involving six DOFs, the sub-aperture maps were precisely aligned and stitched together, as shown in Fig. 8. Compared with the full-aperture map acquired by direct data fusion in Fig. 7 (b), the discontinuity is fully eliminated, and the smoothness is great improved. However, while conducting the characterization by directly subtracting the designed CPP surface from the full-aperture map, the false form error is still maintained to be RMS 220.6 nm. According to Fig. 8 (b), the misalignment-induced error is obvious left. The residual tip-tilt error occurs, and the extra microstructural error indicates the lateral misalignment-induced error, which is closely connected with the CPP surface topography. Based on this, the following registration was further performed, as shown in Fig. 8 (c), and the final form error is RMS 2.6 nm. Although it is close to the theoretical zero value, there still exists the slight deviation.

To find out the reason why the deviation occurs, another comparison simulation was conducted, where the stitching process was removed and only regular characterization was maintained. The designed CPP surface was misaligned with the same random values, and the regular characterization was carried out by registration. According to Fig. 9, the RMS value of the misaligned CPP surface is 542.6 nm. After the registration, the form error is determined to be RMS 1.91×10^{-13} nm. It shows the regular characterization is correct, and also indicates the deviation in Fig. 8 (c) comes from the sub-aperture stitching process. The stitching error is unavoidably transferred to the following characterization stage, and generates the uncertainty of form error evaluation. Considering this, the conventional quality inspection of CPPs is sensitive to the error accumulation.

By contrast, the stitching results by the stitching-embedded characterization method is presented in Fig. 10. By implementing the subtraction between the designed CPP surface and the full-aperture map, the error is tiny enough to be neglected and extremely close to the theoretical zero value, which only comes from the reverse computation itself. Besides, the full-aperture map has been completely aligned with the designed CPP surface. Therefore, the form error can directly serve for the characterization without any following registration.

Furthermore, the influence of the selection of the standard sub-aperture was investigated by the simulation, as shown in Fig. 11. Despite of the different sub-apertures, the characterization error is insensitive to the selection of sub-aperture, which is almost controlled in the order of 10^{-10} nm. The computation error fluctuation is mainly attributed to the different random misalignment value. In summary, the proposed stitching-embedded characterization method is reliable and stable for the quality inspection of CPPs.

4.2. Form error separation

For imprinting CPPs, the removal distribution generation highly depends on the form error separation in the characterization procedure, and its accuracy largely impacts the efficiency of every figuring iteration. To fully investigate this, the simulation in Section 4.1 was further modified by adding the artificial form error on the designed CPP surface to generate the ideal full-aperture map, which is assumed to be the imprinted CPP that contains the form error, as shown in Fig. 12. Then, it was divided into different misaligned sub-aperture maps. In light of the specific requirement of CPPs, the two-dimensional sinusoidal wave was defined as the hypothetical form error to be added, and the expression was,

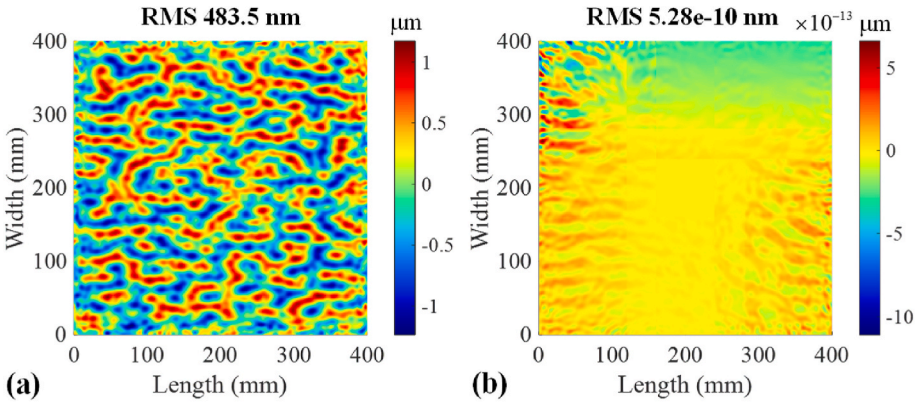

Fig. 10. Simulation results with the proposed stitching-embedded characterization method. (a) Full-aperture map after stitching; (b) Form error by directly subtracting the designed CPP surface from (a).

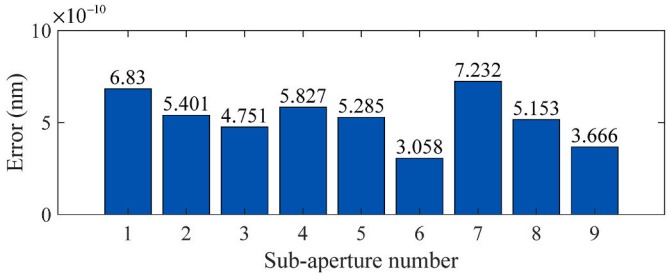

Fig. 11. Influence of the selection of the standard sub-apertures.

$$z(x,y) = A\sin\left(\frac{2\pi}{T}x\right)\sin\left(\frac{2\pi}{T}y\right) \tag{23}$$

where A is the amplitude and T is the spatial wavelength. The RMS of the form error was defined to be approximately 30 nm ($A = 60$ nm and $T = 30$ mm).

Similar to Section 4.1, the form error separation was conducted with both the conventional quality inspection and the proposed stitching-embedded characterization method, and the simulation results are given in Fig. 13. From Fig. 13 (b), the separated form error with the conventional method is RMS 30.82 nm, which is quite close to the nominal value of RMS 30.68 nm. However, compared with Fig. 13 (a), there exists the extra irregular deviation as shown in Fig. 13 (c), which is similar to Fig. 8 (c). This further indicates that the sub-aperture stitching error greatly impacts the following characterization, which is transferred to the form error evaluation and misguides the figuring process.

According to Fig. 13 (d), the form error separated by the stitching-embedded characterization method is more theoretically accurate. The separated form error shows the high fidelity, and the RMS value is 30.69 nm. The difference is only RMS 0.42 nm, and indicates the strong analysis capability of the proposed stitching-embedded characterization method of CPPs, which can provide the more reliable form error evaluation with sub-nanometer accuracy in simulation.

5. Measurement experiment and results

In order to further validate the proposed characterization method in application, the sub-aperture stitching test of the CPP sample fabricated by atmospheric pressure plasma processing (APPP) [7,19] was conducted in our self-developed stitching system, as shown in Fig. 14 (a), which mainly consists of the Shineoptics G150 laser interferometer with the pixel size of 75 μm and the two-axis translational stage. The holder contains the high-precision flat mirror used as the reflector. The size of the designed CPP surface is 320 mm × 320 mm, as shown in Fig. 14 (b). The central topography of 300 mm × 300 mm was imprinted on the planar substrate in a single cycle of APPP, and the transmitted wavefronts were measured. Considering the limited FOV, the size of each sub-aperture map was designed to be 100 mm× 100 mm with the mask for a 6″ aperture interferometer, and the sub-aperture layout is shown in Fig. 14 (c). The whole effective analysis area is 292 mm × 292 mm in the center that exclude the edge effect. With the raster path, all the sub-aperture maps were obtained with the sub-millimeter positioning accuracy (0.01 mm), as shown in Fig. 15. For each sub-aperture map, averaged ten cycles are adopted in phase-shifting, and only the piston and tilt were removed. With the sub-aperture maps, the quality inspection of the CPP sample were both implemented by the conventional and proposed stitching-embedded characterization method.

Fig. 16 gives the quality inspection results of the CPP sample by the conventional method. First, the full-aperture map was obtained by stitching all the sub-aperture maps together, as shown in Fig. 16 (b). For the sake of smaller size of the full-aperture map, the corresponding

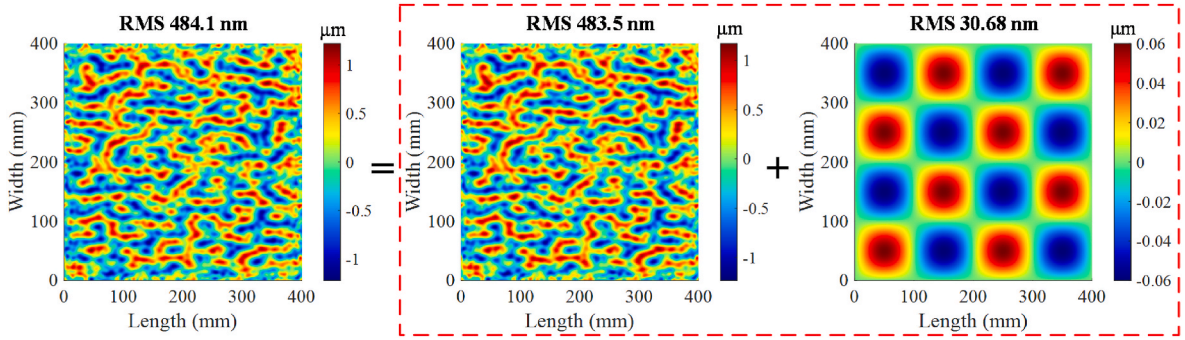

Fig. 12. Generation of the imprinted CPP by adding the sinusoidal form error on the designed CPP surface.

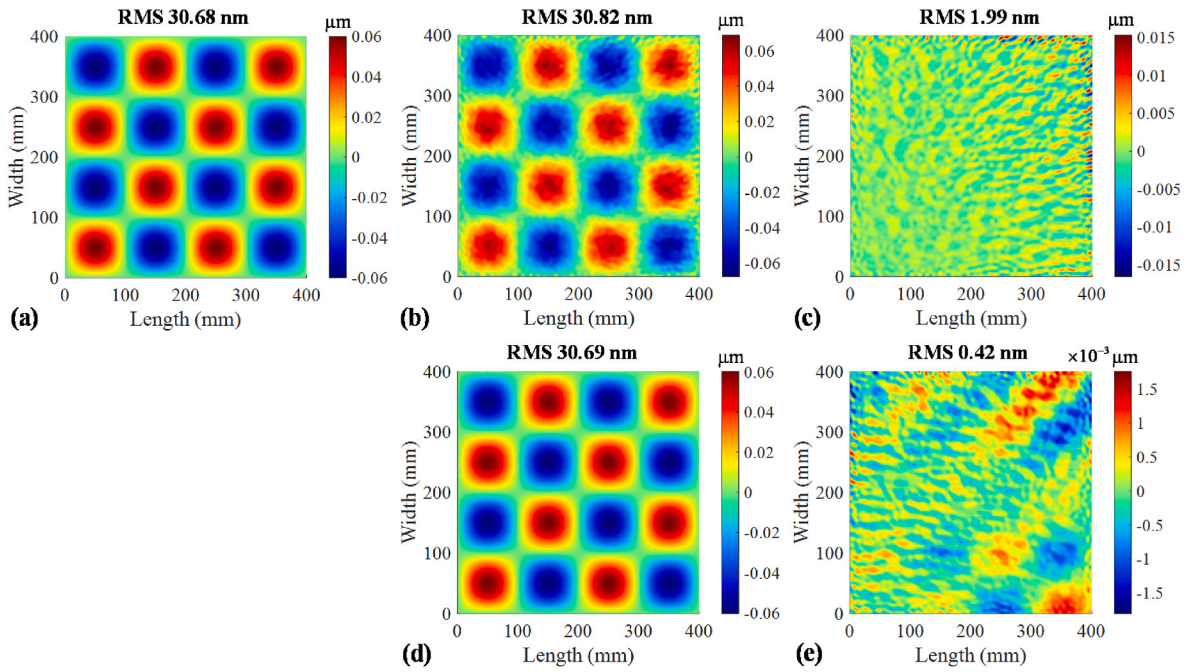

Fig. 13. Comparison of the form error separation with two methods. (a) Hypothetical form error; (b) Separated form error with the conventional quality inspection; (c) Form error deviation with the conventional quality inspection; (d) Separated form error with the proposed method; (c) Form error deviation with the proposed method.

designed CPP surface was automatically searched as given in Fig. 16 (a). Without any registration, the false form error can be acquired by directly subtracting two maps, as shown in Fig. 16 (c). Obviously, there exists the residual misalignment-induced error, which unavoidably misguides the following figuring iteration. Further, the regular characterization with registration was also conducted to adjust the full-aperture map, as shown in Fig. 16 (d). This way, Fig. 16 (e) presents the form error acquired by subtraction, which is determined to be RMS 117.1 nm.

Fig. 17 presents the quality inspection results of the CPP sample by the stitching-embedded characterization method. In this procedure, all the sub-aperture maps were automatically stitched together, as shown in Fig. 17 (b), and aligned with the corresponding partial designed CPP surface. The direct subtraction was implemented to obtain the form error, as shown in Fig. 17 (c). Not surprisingly, the form error is similar to the analysis results by the conventional method, which is RMS 117.5 nm.

In detail, the form error difference is further acquired by conducting the registration and subtraction between Figs. 16(e) and Fig. 17 (c), as shown in Fig. 18, and the RMS value is 8.6 nm. According to the analysis in Section 4, it mainly comes from the error accumulation of the stitching procedure in the quality inspection. Therefore, the RMS value of 117.5 nm acquired by the proposed method can be considered to be more accurate and trustworthy.

From the above analysis, the form error can be precisely determined, and the convergence rate of the single APPP is about 76.5%, which embodies its excellent figuring performance. Note that, the quality inspection of CPPs with two methods were both performed on the same desktop. The time cost of the conventional method is 3.65 min, while it is only 1.74 min for the proposed method. Above all, compared with the conventional quality inspection of CPPs, the proposed method can achieve more reliable form error evaluation with higher efficiency, which avoids redundant multiple-step process that leads to the uncertainty propagation.

6. Conclusions

In this paper, the stitching-embedded characterization method is presented for imprinting large-aperture CPPs. Compared with conventional inspection process, the proposed stitching-embedded characterization method combined the two originally independent stages together, which simplifies the multiple-step analysis procedure. By simulations, the proposed method was validated and proved to be

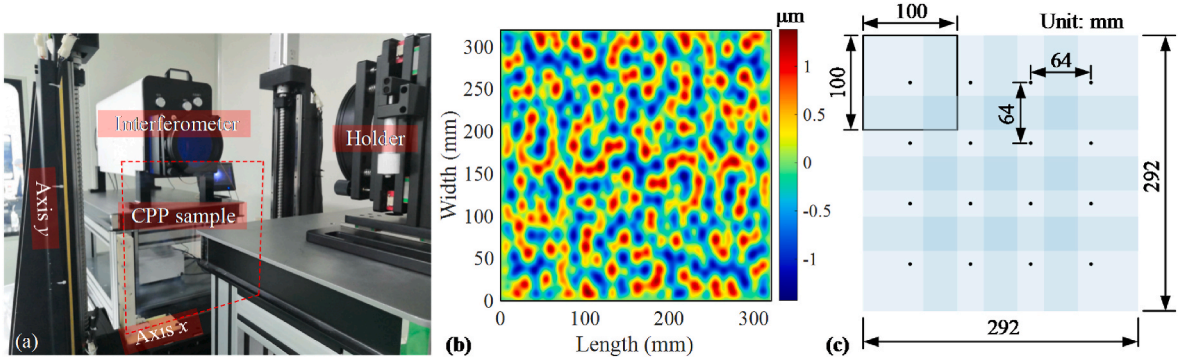

Fig. 14. Details of the sub-aperture stitching test. (a) Stitching system; (b) Designed CPP surface; (c) Sub-aperture layout.

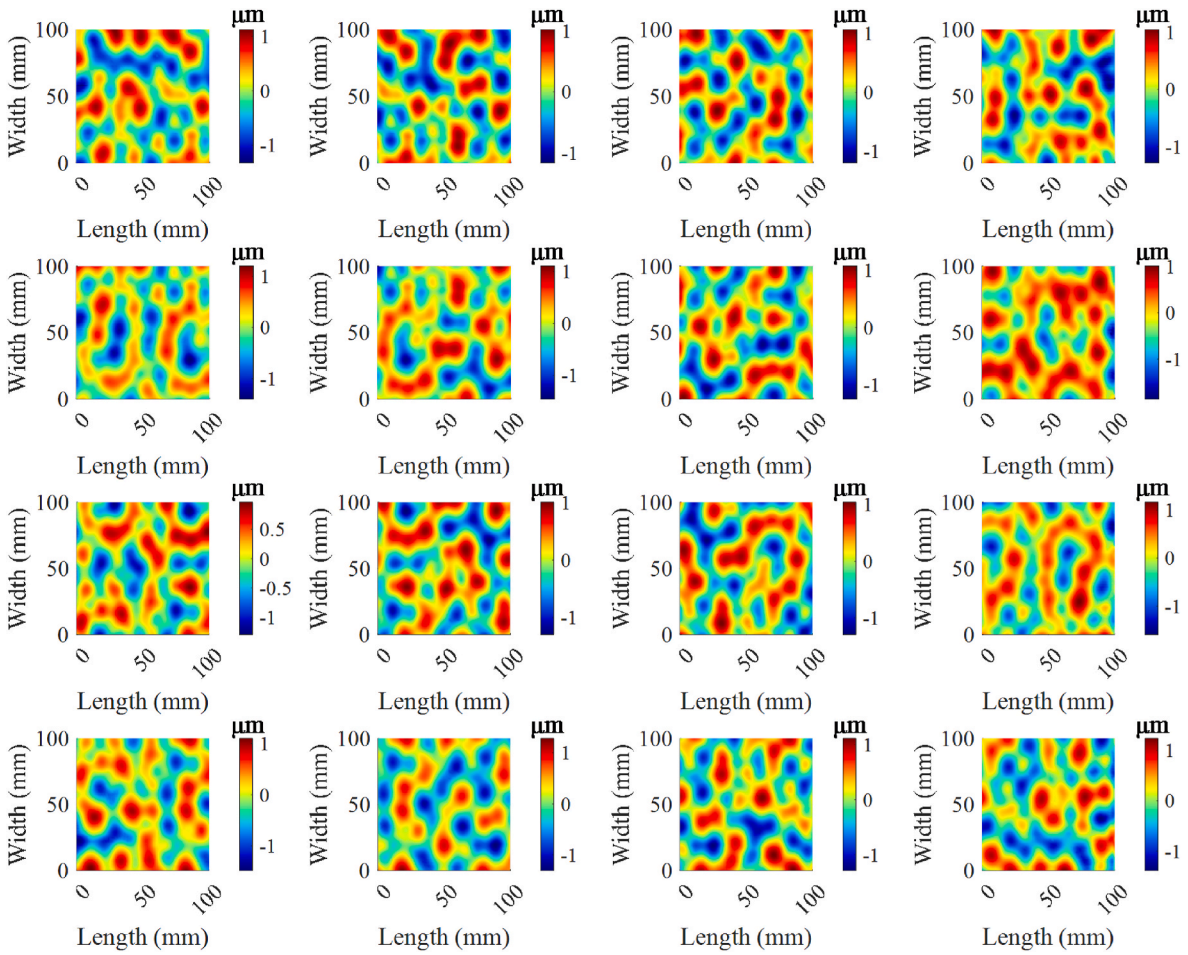

Fig. 15. Sub-aperture maps acquired by the stitching test.

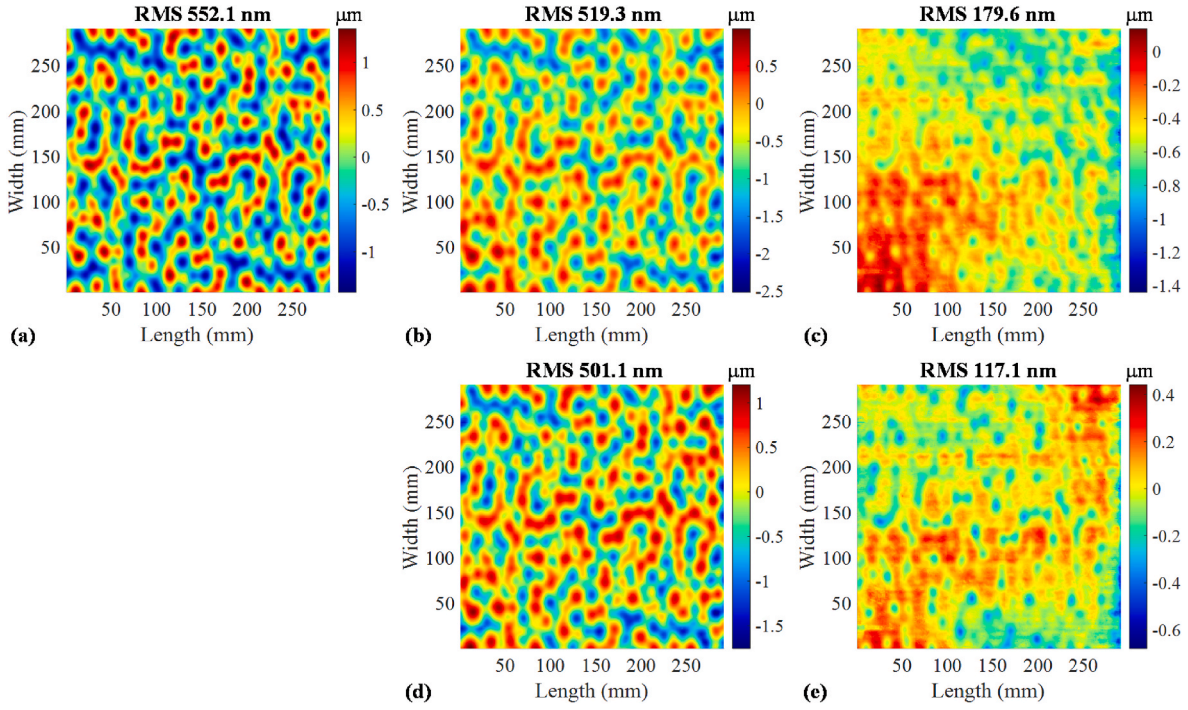

Fig. 16. Quality inspection of the CPP sample by the conventional method. (a) Corresponding designed CPP surface; (b) Stitching results by the complete stitching algorithm; (c) Difference between (a) and (b); (d) Alignment results of (b) after registration with (a); (e) Difference between (a) and (d).

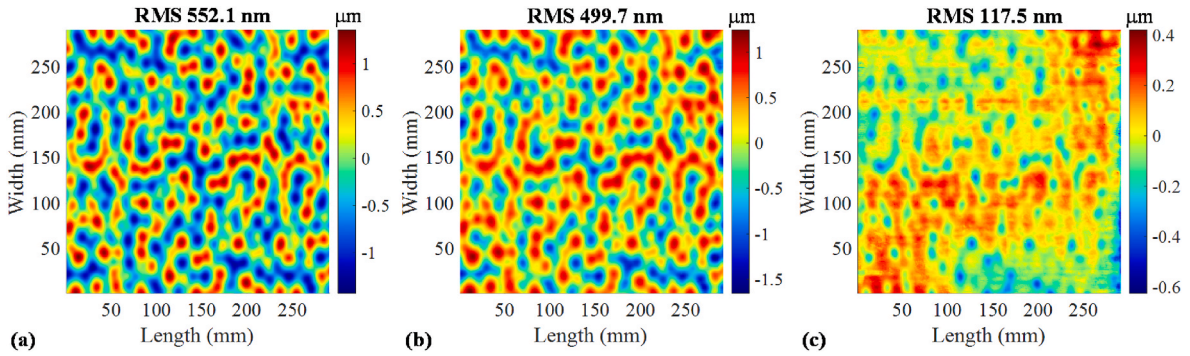

Fig. 17. Quality inspection of the CPP sample by the stitching-embedded characterization method. (a) Corresponding designed CPP surface; (b) Stitching results; (c) Difference between (a) and (b).

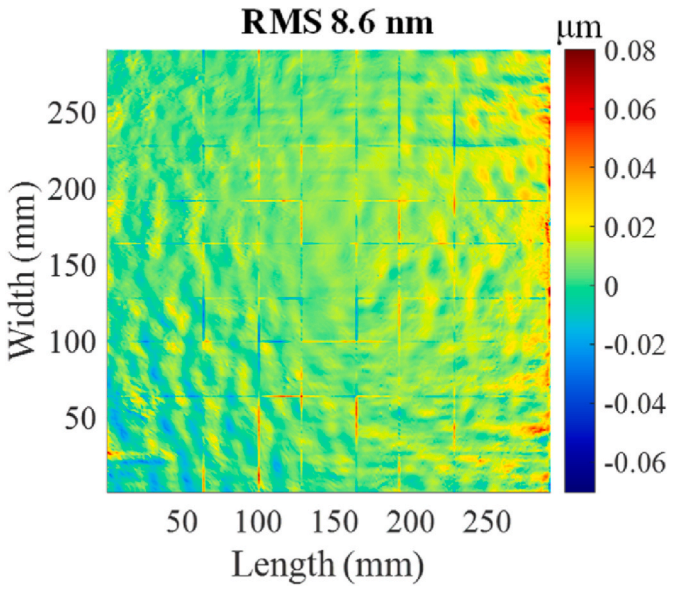

Fig. 18. Form error difference between the two methods.

feasible and reasonable. It is found that the proposed method is capable of separating form error from the imprinted CPPs with higher fidelity and sub-nanometer accuracy in simulation. Finally, the sub-aperture stitching test of the CPP sample was experimentally carried out in our self-developed stitching system. The results indicate that the proposed method can successfully provide one-step characterization with better accuracy and lower time cost. Above all, compared with the conventional method, the proposed stitching-embedded characterization method can achieve more reliable form error evaluation with higher efficiency for the quality inspection of CPPs.

Declaration of competing interest

The authors declare that they have no known competing financial interests or personal relationships that could have appeared to influence the work reported in this paper.

Acknowledgments

The work was supported by the Open Project Program of State Key Laboratory of applied optics (SKLAO2021001A05); National Natural Science Foundation of China (No.51905130); Heilongjiang Provincial Natural Science Foundation of China (No. LH2020E039).

The authors would like to sincerely thank the reviewers for their valuable comments on this work.

References

[1] Oron R, Davidson N, Friesem AA, Hasman E. Continuous-phase elements can improve laser beam quality. Opt Lett 2000;25:939–41.
[2] Menapace JA, Peer AS, Tham GC. Manufacturing high-gradient freeform continuous phase plates (CPPs) using magnetorheological finishing. Optical design and fabrication 2019 (freeform, OFT). Washington, DC: Optica Publishing Group; 2019. JW1A.5.
[3] Chen S, Li S, Dai Y, Peng X, Zhang W. Fast and precise registration of quasi-planar free-form wavefronts. J Opt Soc Am A 2010;27:1655–9.
[4] Menapace JA. Imprinting continuously varying topographical structure onto large-aperture optical surfaces using magnetorheological finishing. Proc Euspen 2007;II:181–4.
[5] Xu M, Dai Y, Xie X, Zhou L, Peng W. Fabrication of continuous phase plates with small structures based on recursive frequency filtered ion beam figuring. Opt Express 2017;25:10765–78.
[6] Zhong B, Deng W, Chen X, Wen S, Wang J, Xu Q. Frequency division combined machining method to improve polishing efficiency of continuous phase plate by bonnet polishing. Opt Express 2021;29:1597–612.
[7] Ji P, Li D, Su X, Qiao Z, Wu K, Song L, et al. Optimization strategy for the velocity distribution based on tool influence function non-linearity in atmospheric pressure plasma processing. Precis Eng 2020;65:269–78.
[8] Tricard M, Dumas P, Menapace J. Continuous phase plate polishing using magnetorheological finishing. SPIE; 2008.
[9] Ye S-w, Yang P, Peng Y-f. A profile measurement method of large aspheric optical surface based on optimal stitching planning. Precis Eng 2016;45:90–7.
[10] Wang R, Li Z-L, Ren M-J, Zhu L-M. A registration-based stitching method for obtaining high-accuracy material removal distribution in the sub-aperture polishing process. Precis Eng 2022;77:251–62.
[11] Néauport J, Ribeyre X, Daurios J, Valla D, Lavergne M, Beau V, et al. Design and optical characterization of a large continuous phase plate for Laser Integration Line and laser Megajoule facilities. Appl Opt 2003;42:2377–82.
[12] Otsubo M, Okada K, Tsujiuchi J. Measurement of large plane surface shapes by connecting small-aperture interferograms. Opt Eng 1994;33.
[13] Chen S, Dai Y, Li S, Shi F, Peng Y. Surface registration-based stitching of quasi-planar free-form wavefronts. Opt Eng 2012;51:063605.
[14] Ji P, Wang B, Li D, Jin Y, Ding F, Qiao Z. Analysis of the misalignment effect and the characterization method for imprinting continuous phase plates. Opt Express 2021;29:17554–72.
[15] Liu MY, Cheung CF, Feng X, Wang CJ, Cao ZC. Any-degrees-of-freedom (anyDOF) registration for the characterization of freeform surfaces. Precis Eng 2020;62:170–80.
[16] Cheung CF, Kong L, Ren M, Whitehouse D, To S. Generalized form characterization of ultra-precision freeform surfaces. CIRP Ann 2012;61:527–30.
[17] Chen S, Dai Y, Nie X, Li S. Parametric registration of cross test error maps for optical surfaces. Opt Commun 2015;346:158–66.
[18] Chen S, Lu W, Chen W, Tie G. Efficient subaperture stitching method for measurement of large area microstructured topography. Opt Laser Eng 2020;127:105974.
[19] Ji P, Li D, Su X, Jin Y, Qiao Z, Wang B, et al. Investigation of the tool influence function neighborhood effect in atmospheric pressure plasma processing based on an innovative reverse analysis method. Opt Express 2021;29:31376–92.